Electronic Supplementary Information

Redox regulation of Ni hydroxides with controllable phase composition towards biomass-derived polyol electro-refinery

Zhuxin Gui[a], Yingshuai Jia[a], Xianping Liao[b], Tianlan Yan[a], Boxu Gao[a], Wenbiao Zhang[ab], Li Chen[c], Qingsheng Gao*[b], Yahong Zhang[a] and Yi Tang*[a]

[a]Department of Chemistry, Shanghai Key Laboratory of Molecular Catalysis and Innovative Materials, Laboratory of Advanced Materials, Fudan University, Shanghai 200433, P. R. China. E-mail: yitang@fudan.edu.cn.

[b]College of Chemistry and Materials Science, Guangdong Provincial Key Laboratory of Functional Supramolecular Coordination Materials and Applications, Jinan University, Guangzhou 510632, P. R. China. E-mail: tqsgao@jnu.edu.cn.

[c]Shanghai Key Laboratory of Green Chemistry and Chemical Processes, East China Normal University, Shanghai 200062, P. R. China.

Table of Contents

Experimental Section

Chemicals

Ni foam (NF, 1.5 mm thickness, 70 pores per inch) was purchased from Suzhou Taili Material Co., Ltd. Nickel sulfate hexahydrate ($NiSO_4 \cdot 6H_2O$, 98.5%), sodium sulfate (Na_2SO_4, 99.0%), potassium hydroxide (KOH, 85.0%), formic acid (FA, 98.0%), glycolic acid (GA, 98.0%), acetic acid (AA, 99.5%), ethylene glycol (EG, 99.0%) and mannitol (MAN, 98.0%) were acquired from Sinopharm Chemical Reagent Co., Ltd. Glycerol (GLY, 99.0%), glyceric acid (GLA, 20 wt% in water) and 1,3-propylene glycol (1,3-PG, 98.0%) were obtained from Aladdin. Tartronic acid (TA, 98.0%), 1,2-propylene glycol (1,2-PG, 99.0%), malonic acid (MA, 99.0%) and Xylitol (XYL, 99.0%) were purchased from Adamas-beta. 3-hydroxypropionic acid (3-HPA, ~30 wt% in water), erythritol (ERY, 97.0%) were obtained from Bidepharm Co., Ltd.

Preparation of catalysts

$Ni(OH)_2$@NFs-*E* were prepared by a facile and simple electrodeposition method with a three-electrode configuration ('*E*' represents the cathodic potential applied during the electrodeposition). 1.5×1.0 cm^2 Ni foam was ultrasonicated for 60 min in anhydrous ethanol and rinsed by deionized water in advance, which was used as the working electrode subsequently. Pt foil and Ag/AgCl (saturated KCl) were applied as the counter and reference electrode, respectively. The electrodeposition was carried out under constant potential (vs. Ag/AgCl) for 600 s in the electrolyte containing 1 M Na_2SO_4 and 0.1 M $NiSO_4$. The as-prepared $Ni(OH)_2$@NFs-*E* were cleaned by deionized water before further characterization and electrochemical measurement.

Physical Characterization

Scanning electron microscopy (SEM) images were obtained by a Zeiss Gemini 300 with a 3.0 kV accelerating voltage. Transmission electron microscopy (TEM) and high-resolution TEM patterns were acquired by a Tecnai G2 F30 FEI. X-ray diffraction (XRD) was carried out on a Bruker D2 with Cu-Kα radiation at 10 kV and 30 mA with a 2θ scanning range of 10° to 100°. Attenuated total reflectance-Fourier transform infrared spectroscopy (ATR-FTIR) experiments were conducted by a Spectrum Two Spectrometer (PerkinElmer) using a diamond ATR detector. X-ray photoelectron spectroscopy (XPS) data were recorded on a Thermo Scientific K-Alpha equipped with Al Kα radiation. H_2 temperature programmed reduction (H_2-TPR) experiments were performed on a Micromeritics AutoChem II 2920 at the heating rate of 5 K/min from 313 to 873 K under the flow of 5% H_2/Ar. Inductively coupled plasma-atomic emission spectrometry (ICP-AES) was carried out on a PE-8000 instrument to evaluate the metal species in the electrolyte after GOR.

Electrochemical measurement

All of the electrochemical measurements were conducted on a typical three-electrode setup with a CHI760E electrochemical workstation, which was divided by proton exchange membrane (Nafion 117). The as-prepared $Ni(OH)_2$@NFs-*E* with geometric area of 1.0×1.0 cm^2 were used as the working electrode, while Pt foil and Ag/AgCl (saturated KCl) presented to be the counter and reference electrode respectively. Cathode chamber was filled with 6 mL of 1 M KOH and anode chamber was filled with 6 mL of 1 M KOH with or without certain concentration of substrate. Specifically, LSV

and CV measurements were performed at the scan rate of 5 mV/s and 2 mV/s. It should be noticed that LSV curves in this report were not compensated with any *iR*-correction at the aim of presenting a holistic characterization without manipulation. GOR performance of the catalysts was evaluated by chronoamperometry (CA) method in the reactor mentioned above under vigorous stirring. The potentials measured throughout this work ($E_{Ag/AgCl}$) could converted to the RHE scale (E_{RHE}) according to the Nernst equation:[1]

$$E_{RHE} = E_{Ag/AgCl} + 0.059 \times pH + 0.198$$

Calculation of turnover frequency (TOF) values for $Ni(OH)_2$@NFs-*E* in GOR were based on the following equation:[2-4]

$$TOF = (j \times N_A)/(n \times F \times \Gamma)$$

Where *j* represents the current density (A/cm^2) measured by LSV, N_A is the Avogadro constant, n stands for the transferred electron number for GOR to produce FA (8 e^-), F is the Faradaic constant (96485 C/mol). Γ is the number of participating active sites for the catalysts, which considers all loaded $Ni(OH)_2$ over NF (measured by H_2-TPR) in this work. Electrochemically active surface areas (ECSA) of $Ni(OH)_2$@NFs-*E* were evaluated by measuring the double-layer capacitance (C_{dl}) at various CV scan rates in the non-faradaic region. *In-situ* Raman spectroscopy was performed on a typical Raman micro-spectrometer (Horiba HR-800) combined with a three-electrode setup and a CHI760E electrochemical workstation. The corresponding Raman spectra were recorded during the CA tests at various potentials and constant time.

Product analysis

The liquid products within the anolyte were separated and analyzed by high performance liquid chromatography (HPLC) equipped with a Bio-Rad Aminex HPX-87H column at 35℃ using 8.0 mM H_2SO_4 aqueous solution as mobile phase under the flow of 0.6 mL/min and detected by a refractive index detector (RID). Calibration curves of standard samples with certain concentrations were established in order to conduct the quantitative analysis of reaction substrates and corresponding oxidation products. The conversion of various substrates, yield and selectivity of formic acid as well as faradaic efficiency were determined by the following equations:

$$\text{Conversion (\%)} = \frac{\text{N (Glycerol Consumed)}}{\text{N (Initial Glycerol)}} \times 100\%$$

$$\text{Yield (\%)} = \frac{\text{N (Formic Acid Formation)}}{3 \times \text{N (Initial Glycerol)}} \times 100\%$$

$$\text{Selectivity (\%)} = \frac{\text{N (Formic Acid Formation)}}{3 \times \text{N (Glycerol Consumed)}} \times 100\%$$

$$\text{Faradaic Efficiency (\%)} = \frac{\text{N (Formic Acid Formation)}}{Q_{total} / (Z \times F)} \times 100\%$$

Where ‘Z’ represents the number of electrons transferred to produce per mole of formic acid (Z = 8/3 for glycerol, Z = 3 for ethylene glycol, Z = 5/2 for erythritol, Z = 12/5 for xylitol and Z = 7/3 for mannitol).

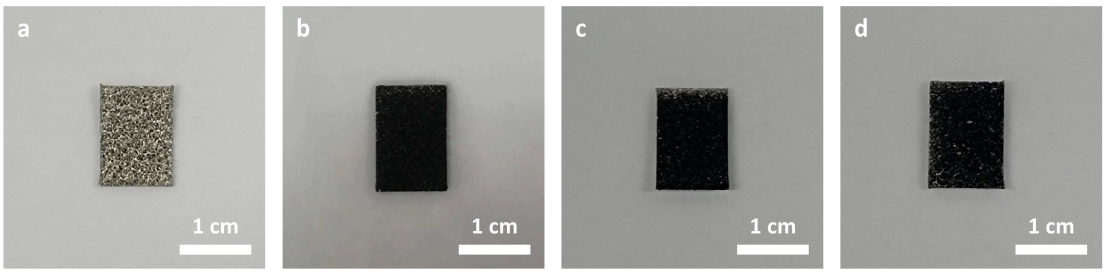

Figure S1. Digital graphs of the as-synthesized catalysts. a) Bare NF, b) $Ni(OH)_2$@NF-0.9, c) $Ni(OH)_2$@NF-1.0 and d) $Ni(OH)_2$@NF-1.2.

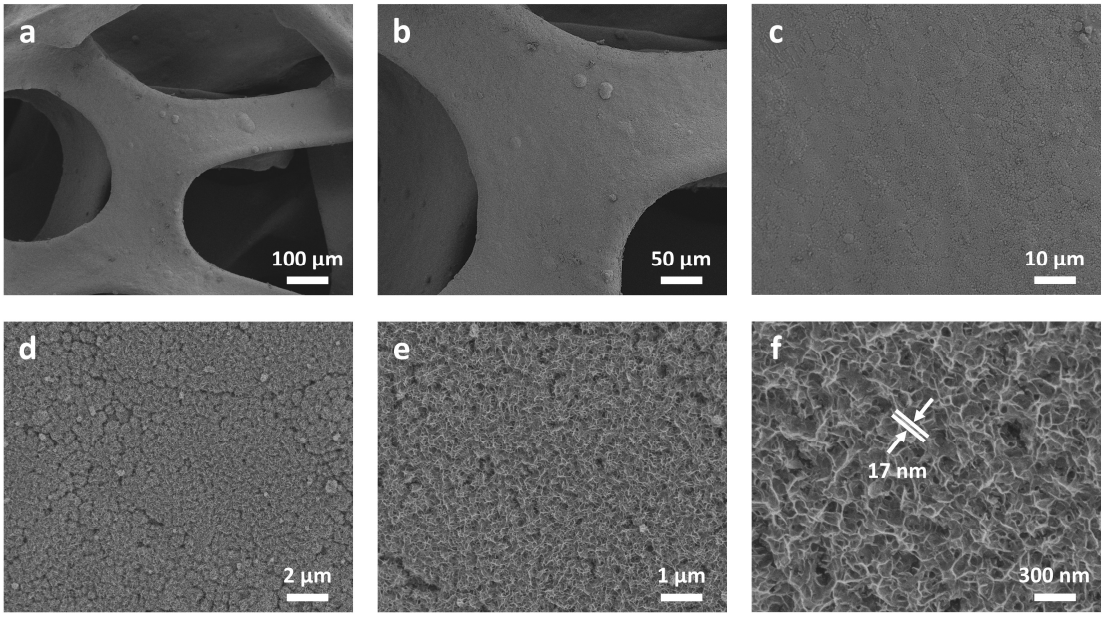

Figure S2. SEM images of $Ni(OH)_2$@NF-0.9.

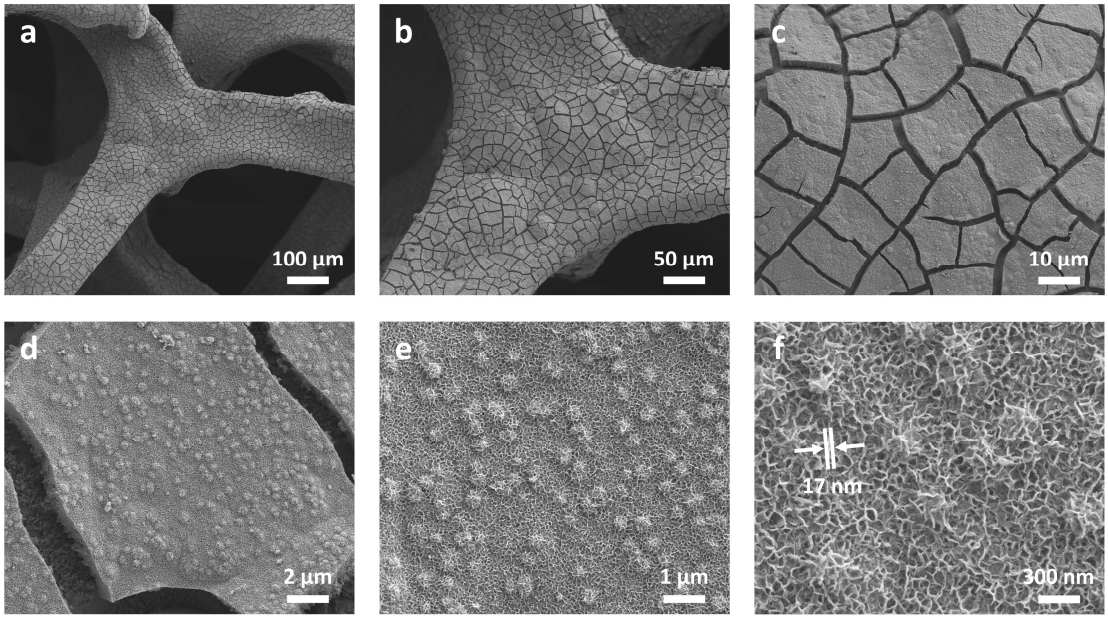

Figure S3. SEM images of $Ni(OH)_2$@NF-1.2.

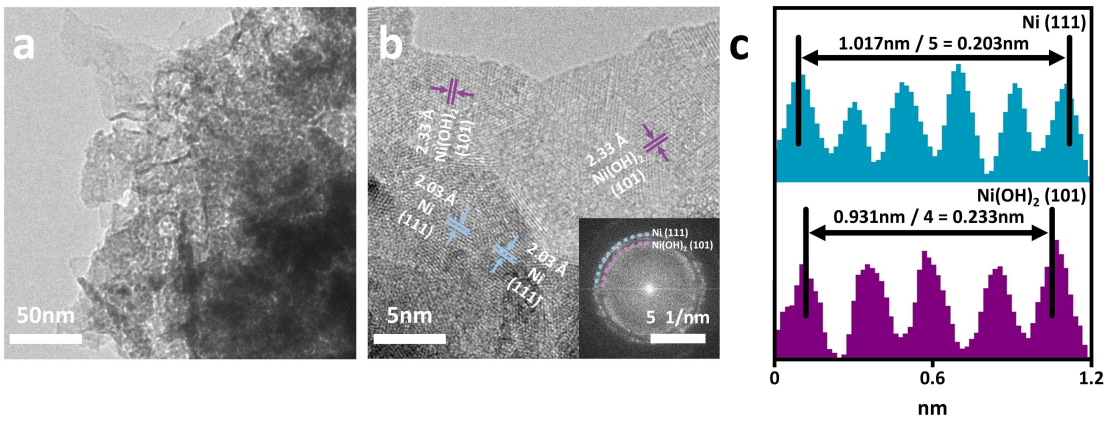

Figure S4. a-b) TEM images of $Ni(OH)_2$@NF-0.9 (inset: Reduced FFT images of HR-TEM). c) Line scan measurements of HR-TEM images.

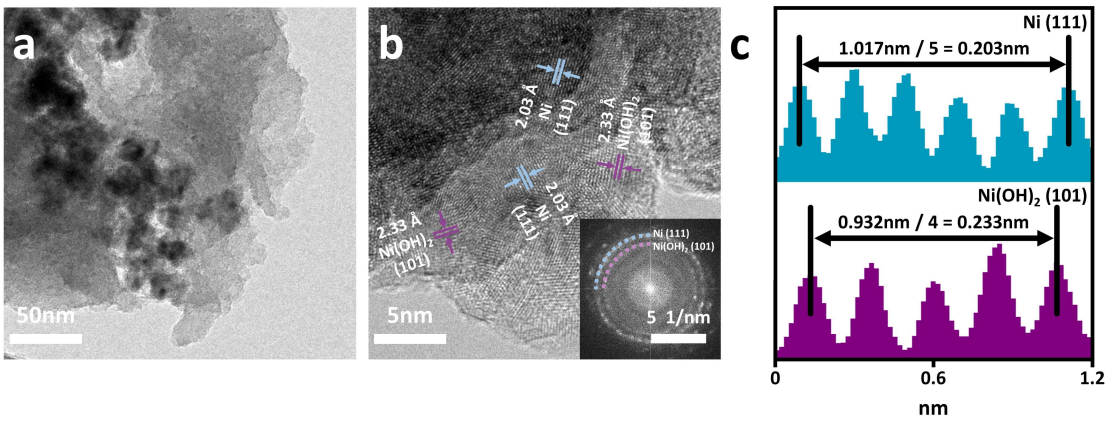

Figure S5. a-b) TEM images of $Ni(OH)_2$@NF-1.2 (inset: Reduced FFT images of HR-TEM). c) Line scan measurements of HR-TEM images.

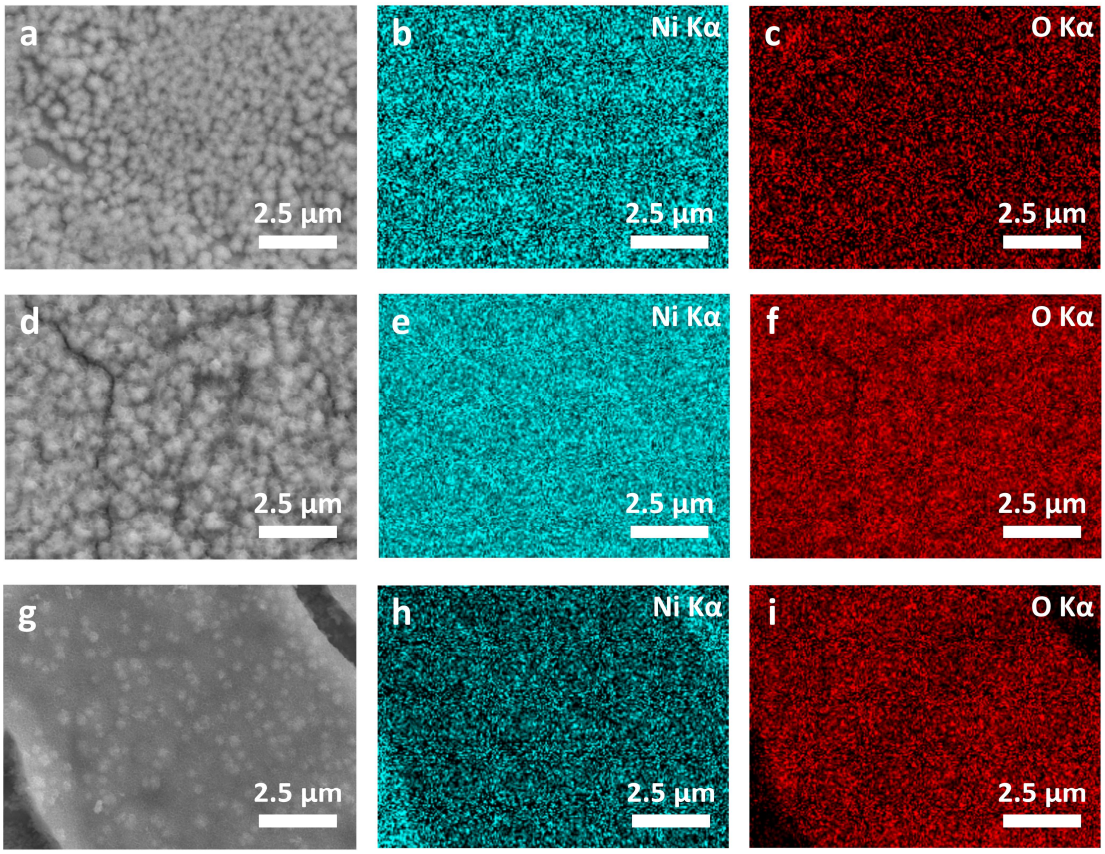

Figure S6. SEM-EDS mapping of a-c) $Ni(OH)_2$@NF-0.9. d-f) $Ni(OH)_2$@NF-1.0. g-i) $Ni(OH)_2$@NF-1.2.

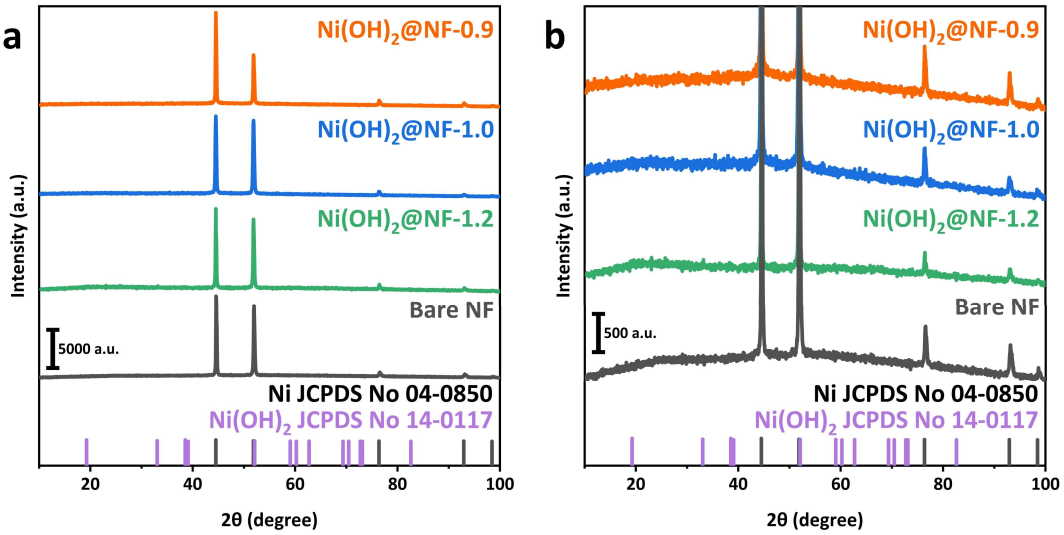

Figure S7. a) XRD patterns of Bare NF and $Ni(OH)_2$@NFs-*E*. b) Enlarged XRD patterns of Bare NF and $Ni(OH)_2$@NFs-*E*.

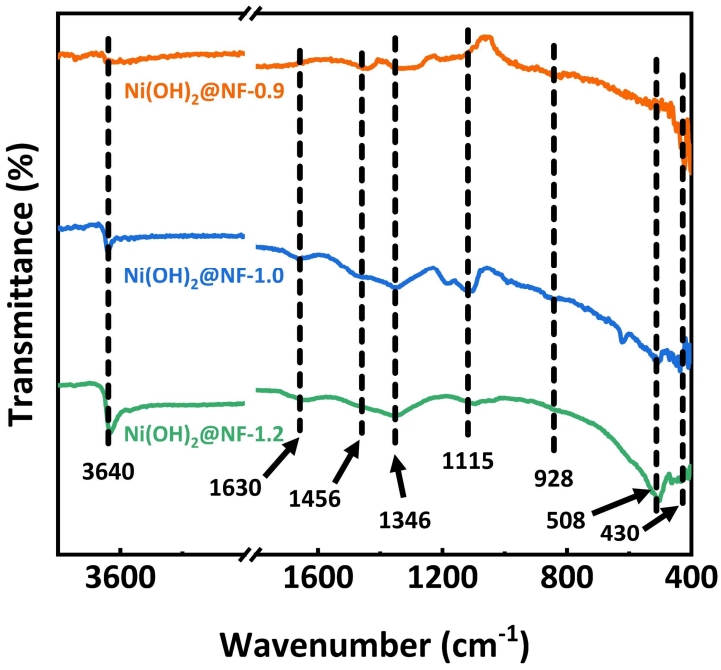

Figure S8. ATR-FTIR spectra of $Ni(OH)_2$@NFs-*E*.

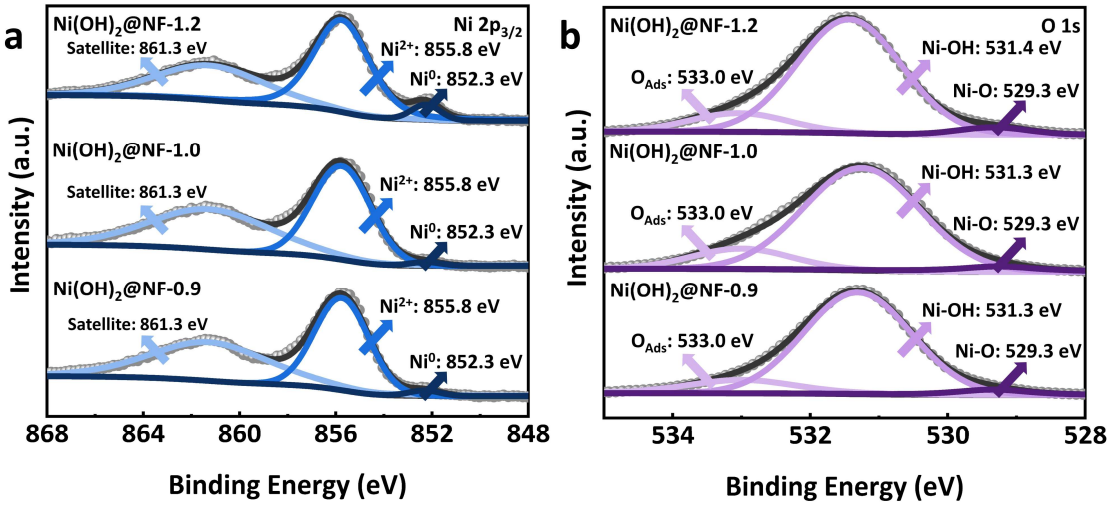

Figure S9. a) Ni $2p_{3/2}$ and b) O 1s XPS spectra of $Ni(OH)_2$@NFs-*E*.

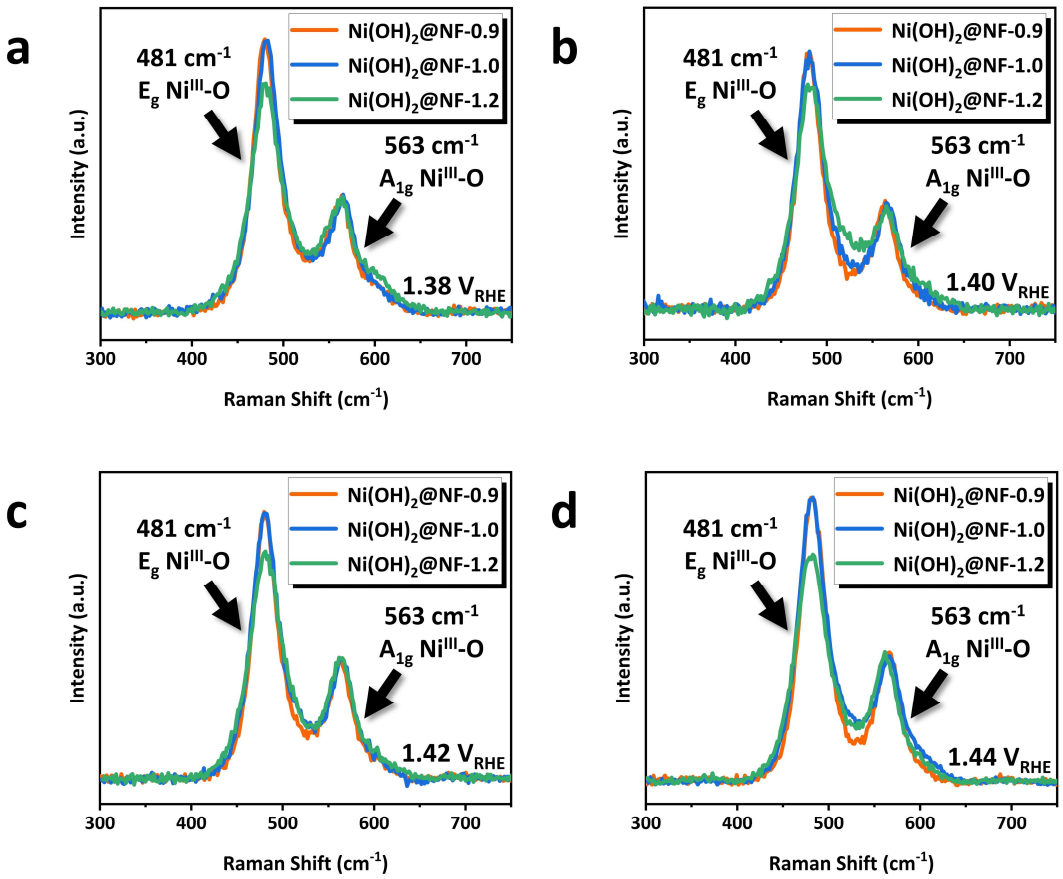

Figure S10. Detailed comparison of the intensity ratio of Ni^{III}-O bands centered at 481 and 563 cm^{-1} from *in-situ* Raman spectra at various potentials for $Ni(OH)_2$@NFs-*E*.

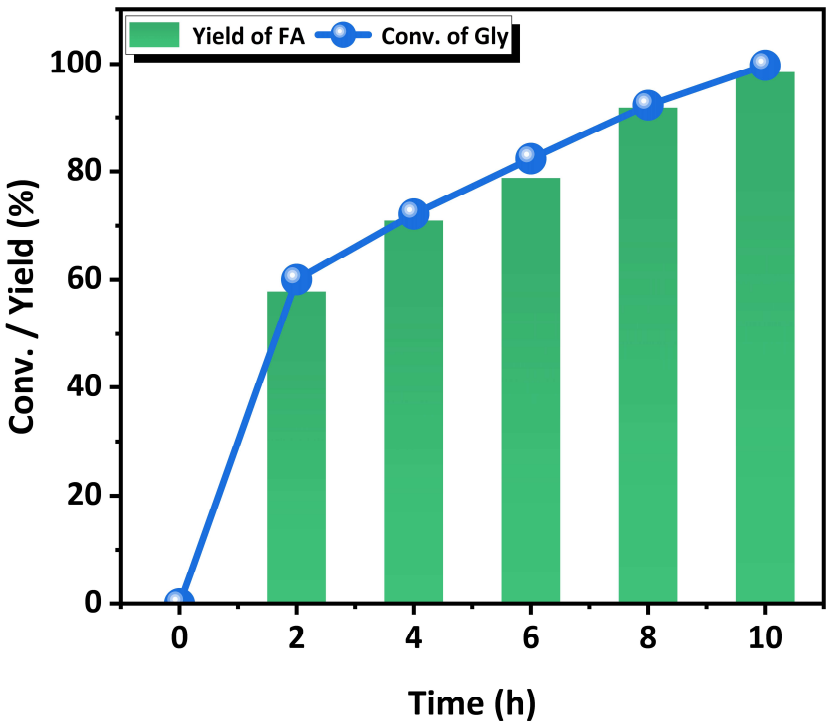

Figure S11. The evolution of GLY conversion and FA yield over $Ni(OH)_2$@NF-1.0 as a function of time.

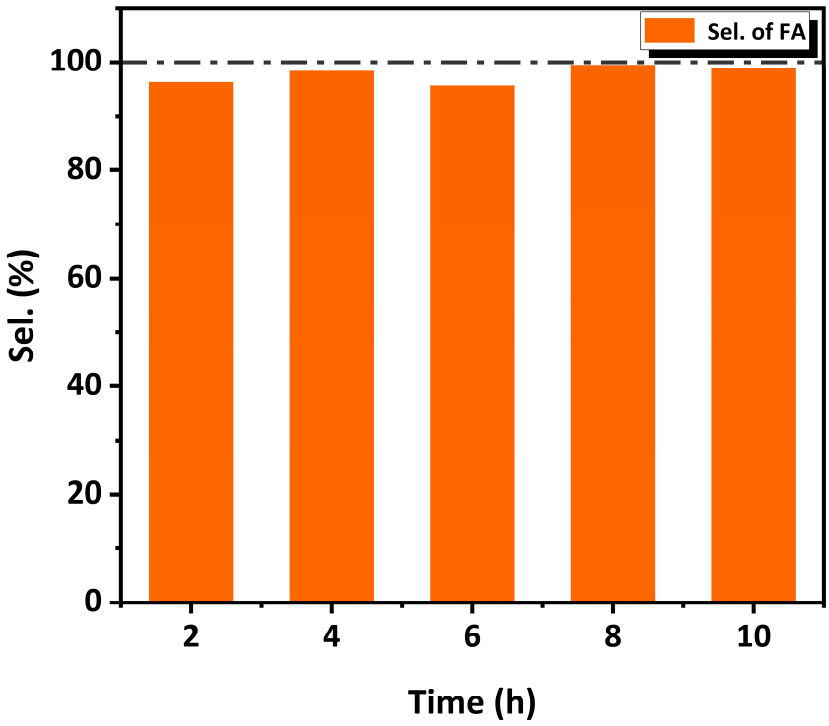

Figure S12. FA selectivity during GOR process over $Ni(OH)_2$@NF-1.0.

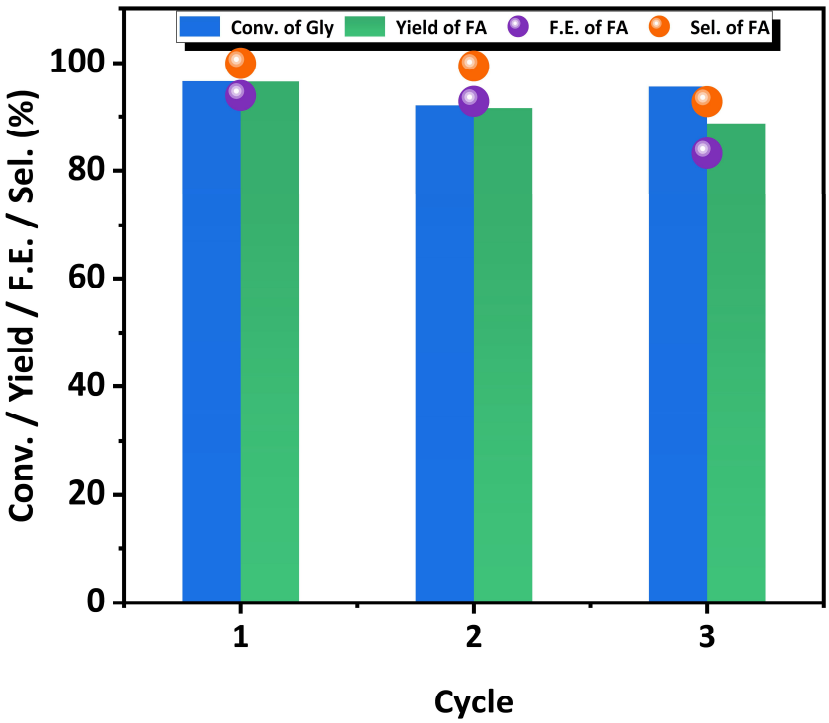

Figure S13. Three successive long-term electrolysis (30 h in total) over $Ni(OH)_2$@NF-1.0.

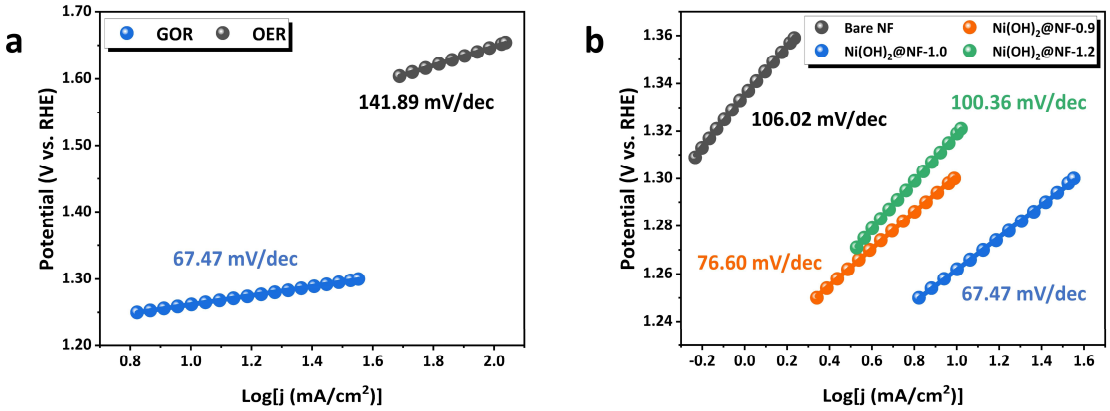

Figure S14. a) Tafel plots derived from LSV curves of $Ni(OH)_2$@NF-1.0 in 1 M KOH with or without the addition of 100 mM GLY. b) Tafel plots derived from LSV curves of $Ni(OH)_2$@NFs-*E* in 1 M KOH with the addition of 100 mM GLY.

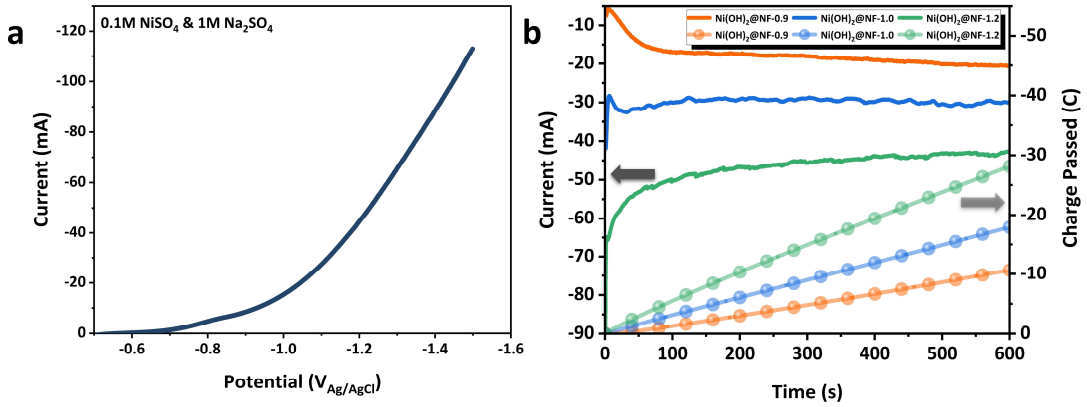

Figure S15. a) LSV curves recorded at the condition of catalysts synthesis. b) Deposition current and charge passed during the synthesis process.

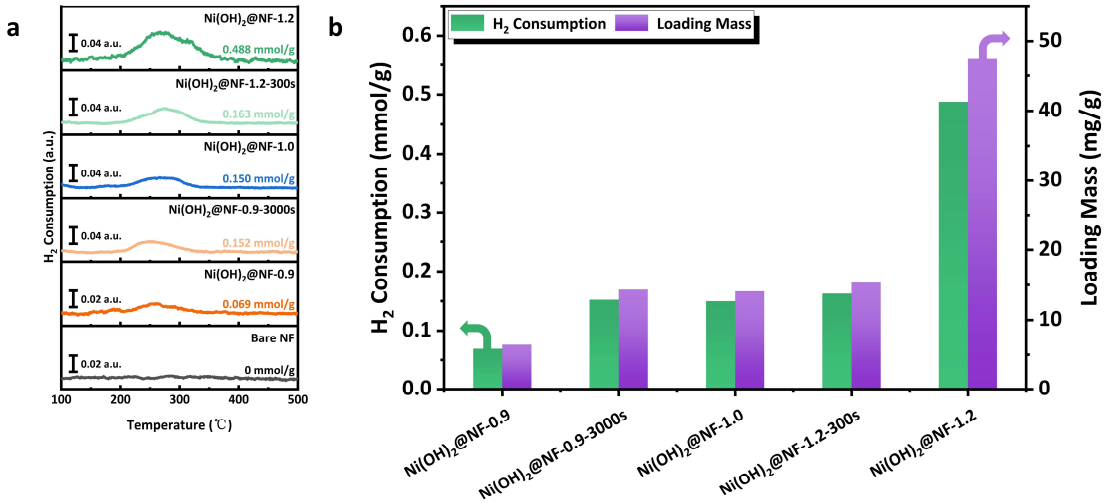

Figure S16. a) H_2-TPR curves for Ni(OH)2@NFs-*E* with different deposition time. b) Calculated H_2 consumption and loading mass of Ni(OH)2@NFs-*E* with controlled deposition time.

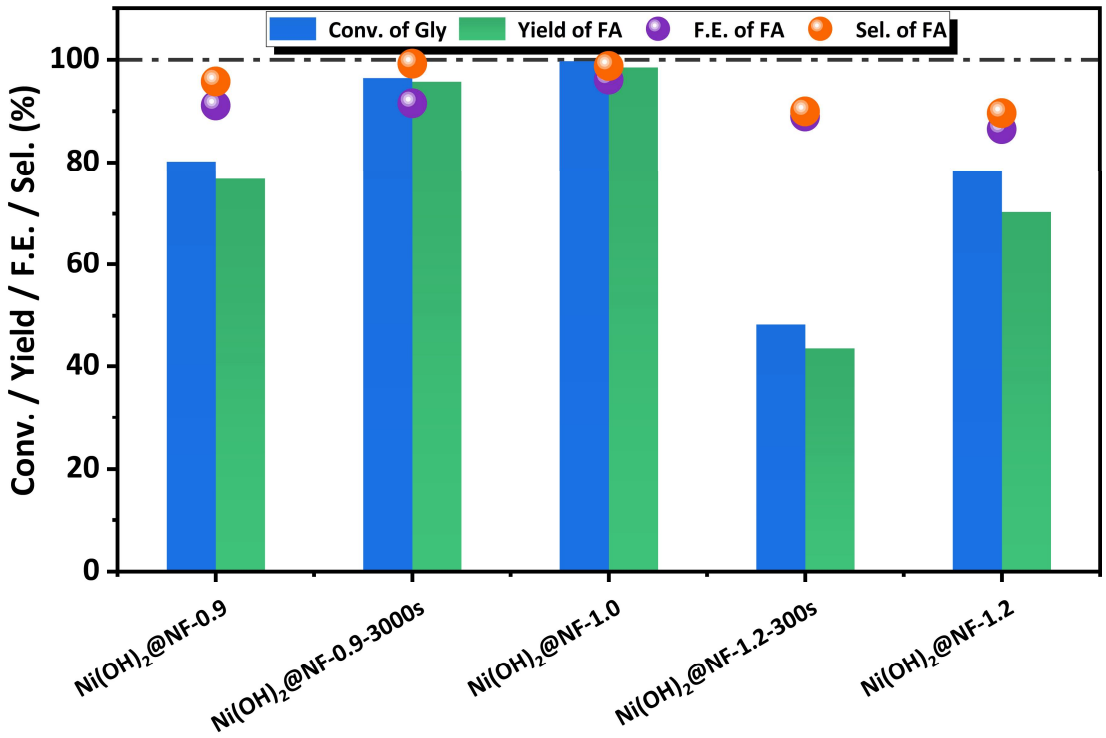

Figure S17. GOR performance (in 1 M KOH & 100 mM GLY at 1.36 V_{RHE} after 10 h) of $Ni(OH)_2$@NFs-*E* with different deposition time.

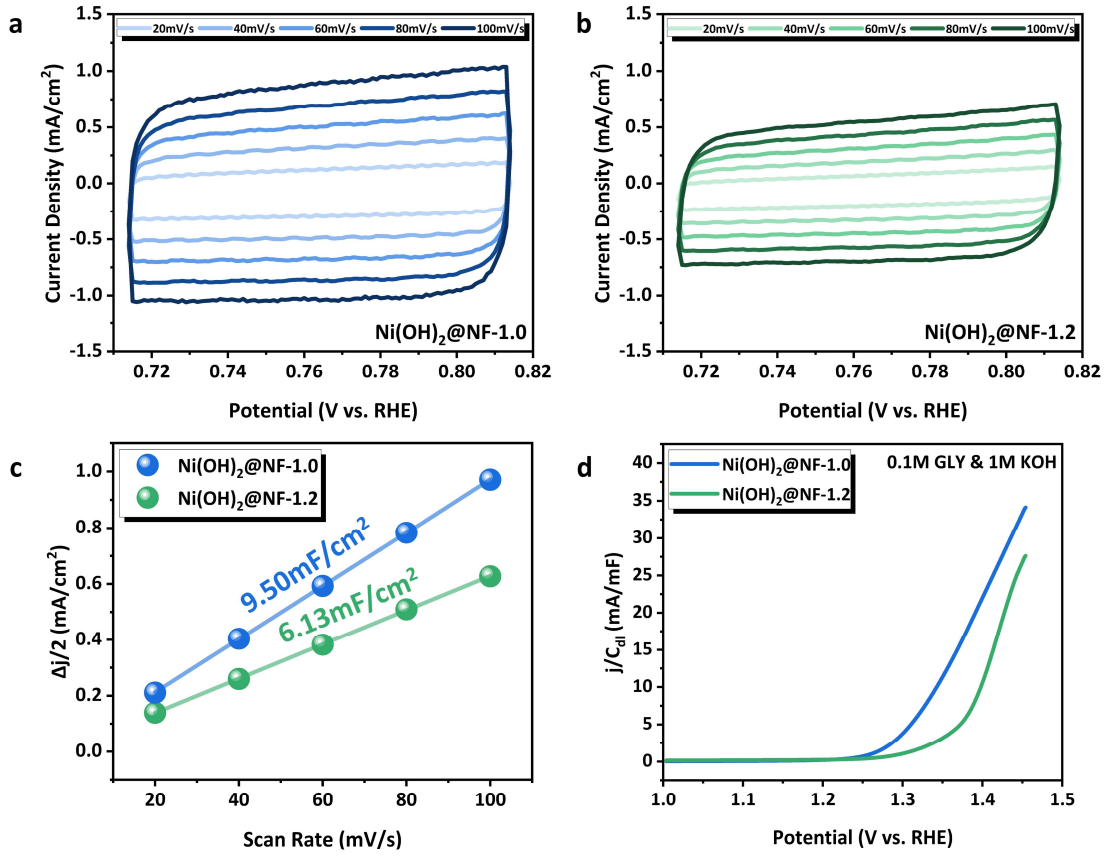

Figure S18. a-b) CV curves of $Ni(OH)_2$@NF-1.0 and $Ni(OH)_2$@NF-1.2 at different scan rates in the non-faradaic region. c) Double-layer capacitances of $Ni(OH)_2$@NF-1.0 and $Ni(OH)_2$@NF-1.2. d) Normalized LSV curves of GOR for $Ni(OH)_2$@NF-1.0 and $Ni(OH)_2$@NF-1.2.

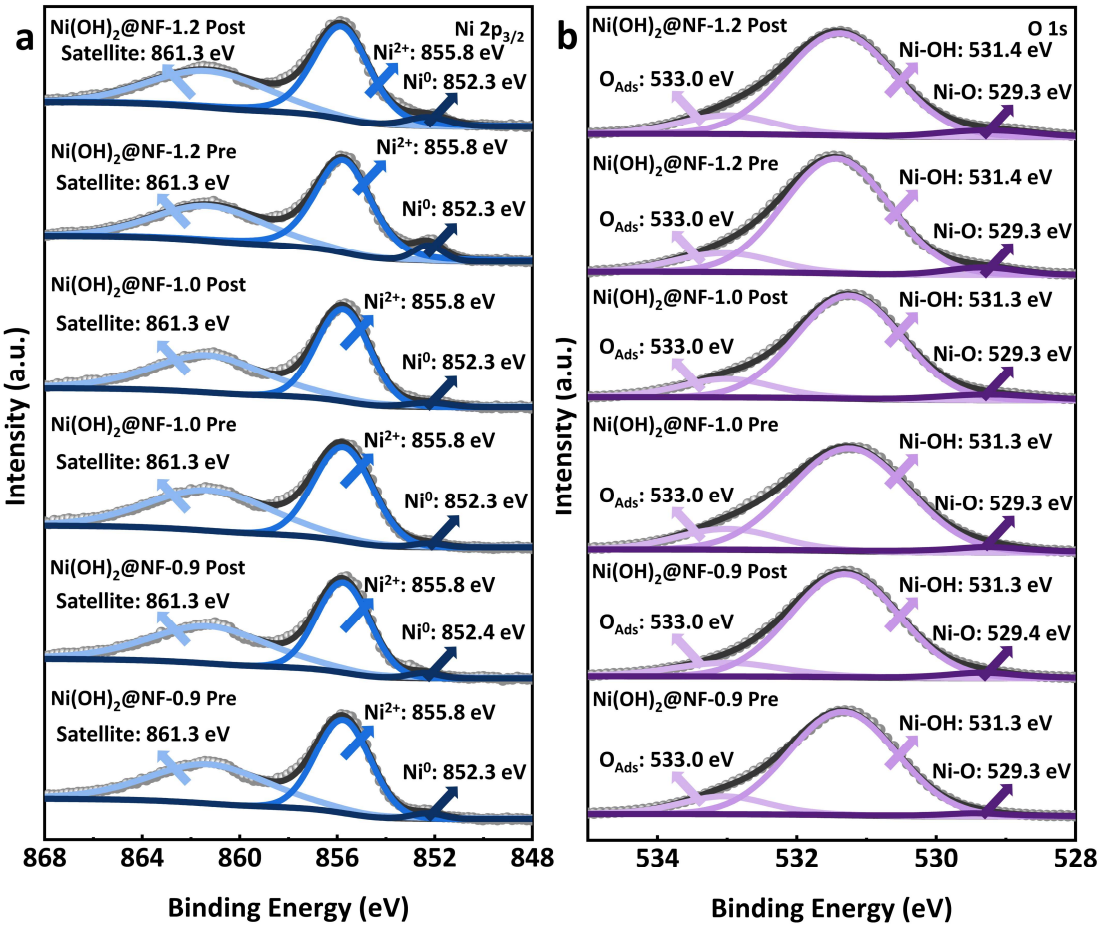

Figure S19. a) Ni $2p_{3/2}$ XPS spectra and b) O 1s XPS spectra of $Ni(OH)_2$@NFs-*E* before and after GOR.

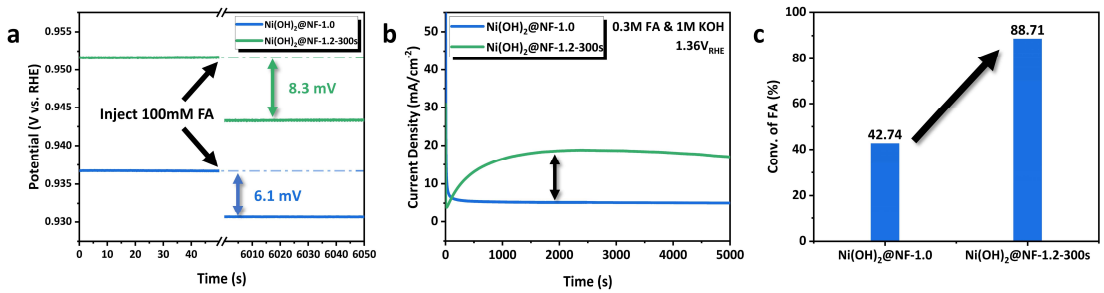

Figure S20. a) The variation of OCP as the function of time with the injection of 100 mM FA for $Ni(OH)_2$@NF-1.0 and $Ni(OH)_2$@NF-1.2-300s. b) I-t curves of FAOR conducted at 1.36 V_{RHE} in 1 M KOH. c) Conversion of FA after 10 h FAOR.

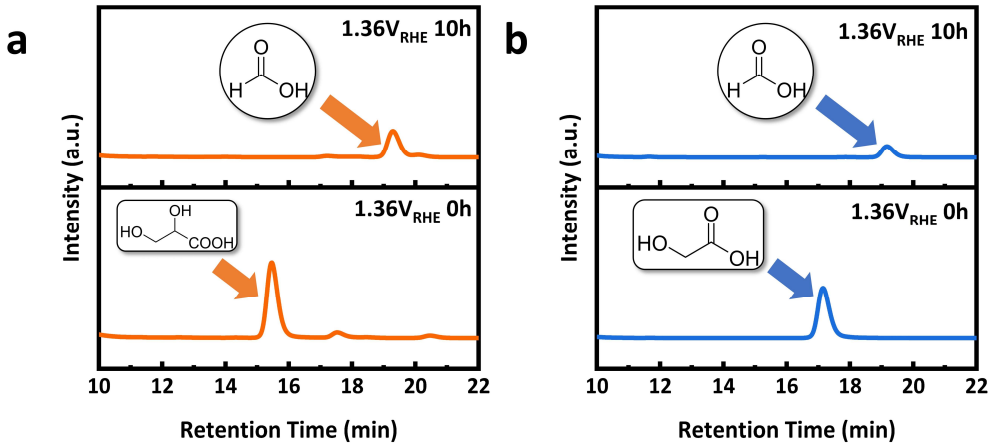

Figure S21. HPLC elution curves of the electrolyte from the electrooxidation of intermediates over $Ni(OH)_2$@NF-1.0 using a) GLA and b) GA as substrates.

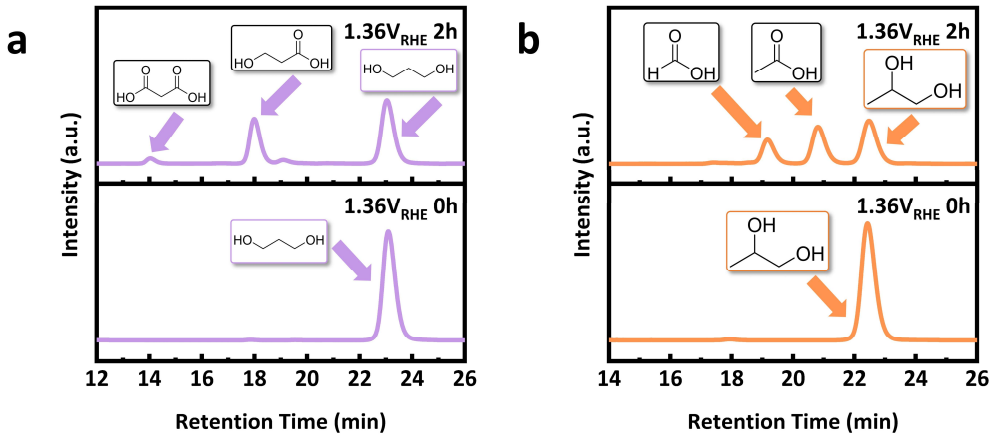

Figure S22. HPLC elution curves of the electrolyte from the electrooxidation of probe molecules over $Ni(OH)_2$@NF-1.0 using a) 1,3-PG and b) 1,2-PG as substrates.

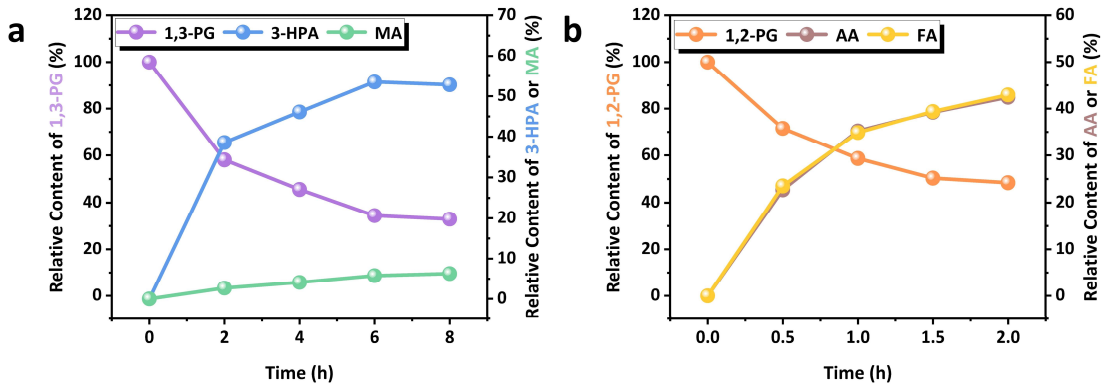

Figure S23. Results of probe reactions over $Ni(OH)_2$@NF-1.0 using a) 1,3-PG and b) 1,2-PG as substrates.

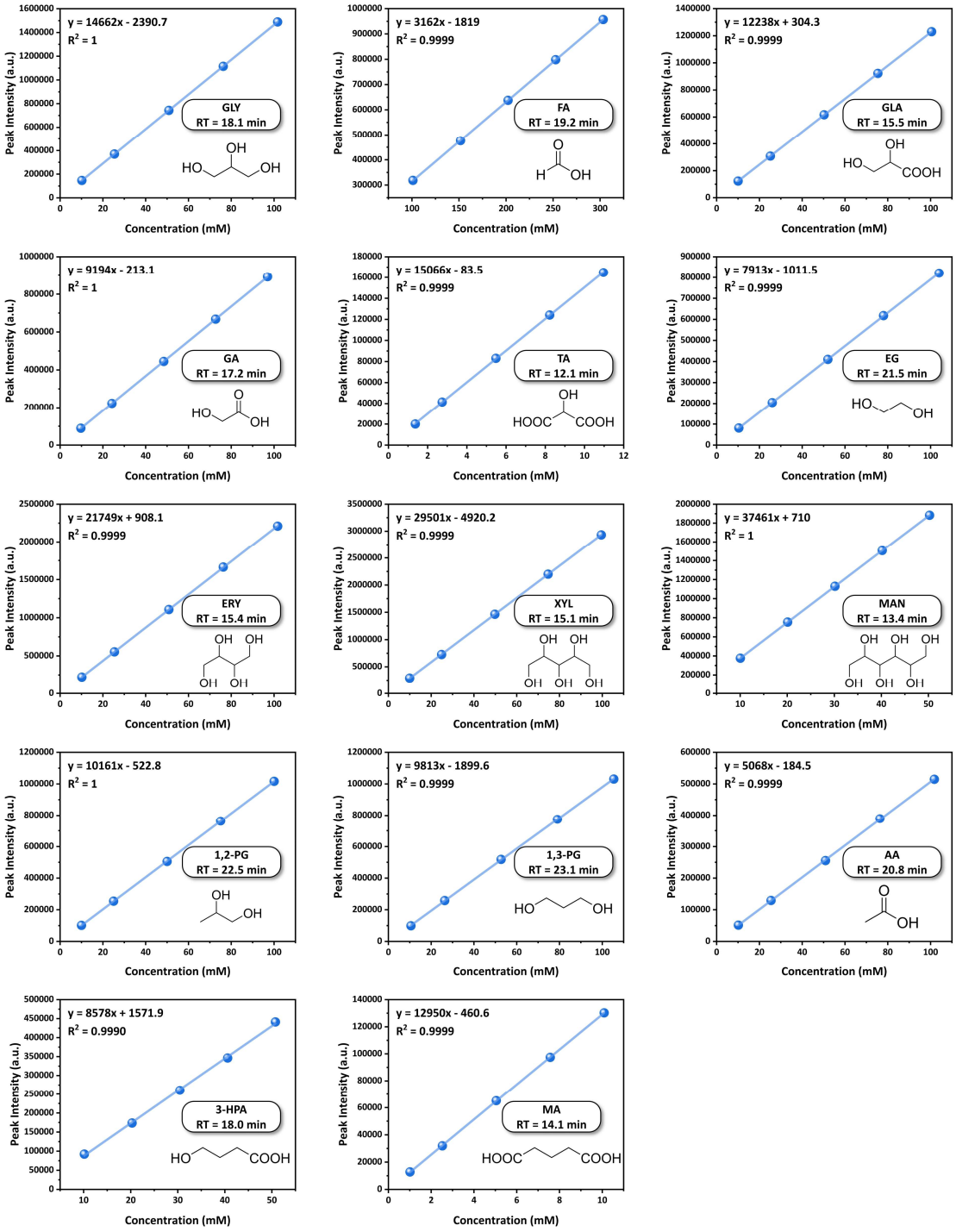

Figure S24. HPLC calibration curves of compounds related to this work.

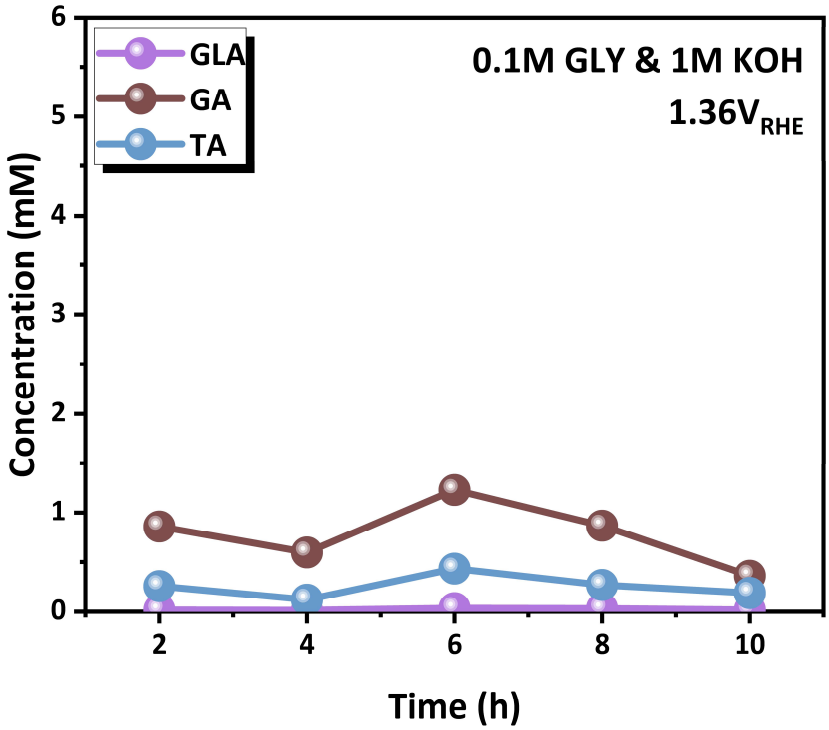

Figure S25. Variation of intermediates concentration during GOR measured by HPLC.

Table S1. Ni content in the anolyte after GOR detected by ICP-AES.

Catalyst	Ni content (ppm)
$Ni(OH)_2$@NF-0.9	Below detection limit (< 0.2 ppm)
$Ni(OH)_2$@NF-1.0	Below detection limit (< 0.2 ppm)
$Ni(OH)_2$@NF-1.2	Below detection limit (< 0.2 ppm)

Reaction Condition: 100 mM GLY; 1.36 V_{RHE}; 10 h.

Table S2. The comparison of 'GOR to FA' performance between $Ni(OH)_2$@NF-1.0 and the state-of-the-art catalysts.

Catalysts	Tafel Slope (mV/dec)	Conditions	Conv. (%)	FA Sel. (%)	F. E. of FA (%)	Ref.
$Ni(OH)_2$@NF-1.0	67.5	1.36 V_{RHE}; 0.1 M GLY; 1 M KOH.	~100	98.8	96.1	This work.
$NiCo_2O_4$/NF	73.0	1.40 V_{RHE}; 0.1 M GLY; 1 M KOH.	~20	93.7	89.9	5
S-CuO/CF	108	1.35 V_{RHE}; 0.1 M GLY; 1 M KOH.	~30	95.1	95.7	6
$Ni(OH)_2$/NF	/	1.50 V_{RHE}; 0.1 M GLY; 2 M LiOH.	/	/	81.3	7
NiVRu-LDHs/NF	102.7	1.40 V_{RHE}; 0.1 M GLY; 1 M KOH.	/	/	~97	8
SA-Bi/Co_3O_4	76.5	1.35 V_{RHE}; 0.1 M GLY; 1 M KOH.	~20	97	97	9
NiCo Hydroxide	68.8	1.62 V_{RHE}; 0.1 M GLY; 1 M KOH.	~89	84	94.3	10
NiCo$(OH)_2$@HOS/NF	35.0	1.35 V_{RHE}; 0.1 M GLY; 1 M KOH.	~90	81.8	~74	11
CoCuMnMoNi High Entropy Alloy	53.5	1.32 V_{RHE}; 0.1 M GLY; 1 M KOH.	/	/	~93	12
Ru-NiP/N-C/NF	86.0	1.45V_{RHE}; 0.1 M GLY; 1 M KOH.	~90	~80	93	13
Cu-CuS/BM	/	1.45V_{RHE}; 0.1 M GLY; 0.1 M KOH.	~40	86.0	90.4	14
Mn-$CoSe_2$/CFC	157.1	1.27V_{RHE}; 0.1 M GLY; 1 M KOH.	/	/	~95	15
$ZnFe_xCo_{2-x}O_4$	163.0	1.62V_{RHE}; 0.5 M GLY; 1 M KOH.	~36	69.5	~50	16
Ni_xB	/	1.80V_{RHE}; 0.1 M GLY; 1 M KOH.	73.0	80.0	/	17
CuNi/ACF	/	1.47V_{RHE}; 0.1 M GLY; 0.1 M KOH.	/	97.4	/	18
$CuCo_2O_4$ Spinel Oxide	/	1.30V_{RHE}; 0.1 M GLY; 0.1 M KOH.	79.7	80.6	89.1	19
Ni-Pd/C		1.55V_{RHE}; 0.1 M GLY; 1 M KOH.	73.1	~98	98	20
Ni-Mo-N/CFC	87.0	1.35V_{RHE}; 0.1 M GLY; 1 M KOH.	~100	92.5	~97	21

Table S3. The amount of Ni hydroxides loaded over NF and TOF values of GOR for $Ni(OH)_2$@NFs-*E*.

Catalyst	Catalytic species content (mg/cm^2)[a]	TOF ($\times 10^{-3}$ s^{-1})
$Ni(OH)_2$@NF-0.9	0.88	7.02
$Ni(OH)_2$@NF-1.0	1.93	7.86
$Ni(OH)_2$@NF-1.2	6.48	0.44

[a]The calculated TOF values were based on the total $Ni(OH)_2$ loaded over NF at a geometric area of 1.0 cm^2 measured by H_2-TPR and the current density tested by LSV.

Table S4. Surface content of Ni species over $Ni(OH)_2$@NFs-*E* before and after GOR measured by XPS.

Catalyst	Content (%)	
	Ni^{2+}	Ni^0
$Ni(OH)_2$@NF-0.9-Pre	96.8	3.2
$Ni(OH)_2$@NF-0.9-Post	96.8	3.2
$Ni(OH)_2$@NF-1.0-Pre	97.8	2.2
$Ni(OH)_2$@NF-1.0-Post	96.6	3.4
$Ni(OH)_2$@NF-1.2-Pre	93.2	6.8
$Ni(OH)_2$@NF-1.2-Post	93.3	6.7

Supplementary References

1 S. Q. Niu, S. W. Li, Y. C. Du, X. J. Han and P. Xu, *ACS. Energy Lett.*, 2020, **5**, 1083-1087.

2 M. R. Gao, W. C. Sheng, Z. B. Zhuang, Q. R. Fang, S. Gu, J. Jiang and Y. S. Yan, *J. Am. Chem. Soc.*, 2014, **136**, 7077-7084.

3 S. Anantharaj, P. E. Karthik and S. Kundu, *Catal. Sci. Technol.,* 2017, **7**, 882.

4 M. Nazari and M. Ghaemmaghami, *ChemSusChem*, 2023, **16**, e202202126.

5 W. S. Luo, H. Tian, Q. Li, G. Meng, Z. W. Chang, C. Chen, R. X. Shen, X. Yu, L. B. Zhu, F. T. Kong, X. Z. Cui and J. L. Shi, *Adv. Funct. Mater.*, 2023, 2306995.

6 R. Y. Fan, X. J. Zhai, W. Z. Qiao, Y. S. Zhang, N. Yu, N. Xu, Q. X. Lv, Y. M. Chai and B. Dong, *Nano-Micro Lett.*, 2023, **15**, 190.

7 J. X. Wu, J. L. Li, Y. F. Li, X. Y. Ma, W. Y. Zhang, Y. M. Hao, W. B. Cai, Z. P. Liu and M. Gong, *Angew. Chem. Int. Ed.*, 2022, **61**, e202113362.

8 Q. Z. Qian, X. Y. He, Z. Y. Li, Y. X. Chen, Y. F. Feng, M. Y. Cheng, H. K. Zhang, W. T. Wang, C. Xiao, G. Q. Zhang and Y. Xie, *Adv. Mater.*, 2023, **35**, 2300935.

9 Y. Wang, Y. Q. Zhu, Z. H. Xie, S. M. Xu, M. Xu, Z. Z. Li, L. N. Ma, R. X. Ge, H. Zhou, Z. H. Li, X. G. Kong, L. R. Zheng, J. H. Zhou and H. H. Duan, *ACS Catal.*, 2022, **12**, 12432-42433.

10 Z. Y. He, J. W. Hwang, Z. H. Gong, M. Z. Zhou, N. Zhang, X. W. Kang, J. W. Han and Y. Chen, *Nat. Commun.*, 2022, **13**, 3777.

11 Y. H. Pei, Z. F. Pi, H. Zhong, J. Cheng and F. M. Jin, *J. Mater. Chem. A.*, 2022, **10**, 1309-1319.

12 L. F. Fan, Y. X. Ji, G. X. Wang, J. X. Chen, K. Chen, X. Liu and Z. H. Wen, *J. Am. Chem. Soc.*, 2022, **144**, 7224-7235.

13 Y. Xu, T. T. Liu, K. K. Shi, H. J. Yu, K. Deng, X. Wang, Z. Q. Wang, L. Wang and H. J. Wang, *J. Mater. Chem. A.*, 2022, **10**, 20365-20374.

14 J. W. Du, Y. Qin, T. Dou, J. M. Ge, Y. P. Wang, X. H. Zhao, F. Z. Zhang and X. D. Lei, *ACS. Appl. Nano Mater.*, 2022, **5**, 10174-10182.

15 L. F. Fan, Y. X. Ji, G. X. Wang, Z. F. Zhang, L. C. Yi, K. Chen, X. Liu and Z. H. Wen, *J. Energy Chem.*, 2022, **72**, 424-431.

16 H. B. Wan, C. C. Dai, L. J. Jin, S. Z. Luo, F. X. Meng, G. Chen, Y. Duan, C. T. Liu, Q. F. Xu, J. M. Lu and Z. C. Xu, *ACS. Appl. Mater. Interfaces*, 2022, **14**, 14293-14301.

17 S. Cychy, S. Lechler, Z. J. Huang, M. Braun, A. C. Brix, P. Blumler, C. Andronescu, F. Schmid, W. Schuhmann and M. Muhler, *Chin. J. Catal.*, 2021, **42**, 2206-2215.

18 J. L. Zhang and Y. Shen, *J. Electrochem. Soc.*, 2021, **168**, 084510.

19 X. T. Han, H. Y. Sheng, C. Yu, T. Walker, G. Huber, J. S. Qiu and S. Jin, *ACS Catal.*, 2020, **10**, 6741-6752.

20 M. Houache, R. Safari, U. Nwabara, T. Rafaideen, G. Botton, P. Kenis, S. Baranton, C. Coutanceau and E. Baranova, *ACS. Appl. Energy Mater.*, 2020, **3**, 8725-8738.

21 Y. Li, X. F. Wei, L. S. Chen, J. L. Shi and M. Y. He, *Nat. Commun.*, 2019, **10**, 5335.